

Chapter 8

New Kinetic Models and Their Atmospheric Implications

Introduction

This chapter will focus on utilizing the various results obtained in the previous chapters in order to ascertain their atmospheric implications. One of the objectives of this thesis is to design and implement a full kinetic sub-ultrafine (< 4 nm diameter) aerosol nucleation model and to extend this model to a full aerosol nucleation model that incorporates particles up to 30 nm diameter. This model will not rely on physical properties that are extrapolated from bulk properties used in other models¹⁻⁴, nor will it assume an initial distribution of pre-existing particles that are commonly used in many other nucleation models.⁵⁻¹⁰ In contrast, this kinetic aerosol model (KAM) is guided by very high level *ab initio* calculations as explained above, measured rate constants and collision theory. One can consider KAM to be a unique model due to its simplicity and the absence of any empirical bulk thermodynamic approximations, fits and relations. There are two models: a minor KAM (KAM-) which calculates only sub-ultrafine particles under 4 nm diameter and a major KAM (KAM+) which calculates particles up to and beyond 4 nm.

The thermodynamic results calculated by *ab initio* and DFT methods will be used in Equation 2-59 to examine how the formation of higher hydrates will influence the homogeneous nucleation rate. Also, a propagation of error (Equation 2-60) on Equation 2-59 will be performed to examine its high non-linear behavior.

Re-Examination of the Modified Nucleation Rate

This section will examine how the C' term (Equation 2-59) will influence the homogenous nucleation rate J (Equation 2-58). As mentioned in Chapter 2 there have been a number of serious problems with the conventional homogenous nucleation theory. Conventional homogenous nucleation theory includes a modification to the classical

homogeneous nucleation theory, which includes the incorporation of higher hydrates in the $\text{H}_2\text{SO}_4\text{-H}_2\text{O}$ system.¹ The primary reason for the incorporation of higher hydrates was to estimate the influence that the presence of higher hydrates had on the nucleation rate. We will show that classical nucleation theory is still valid and can be corrected for its problems in underestimating (by orders of magnitude) the rate of formation of nuclei in the $\text{H}_2\text{SO}_4\text{-H}_2\text{O}$ system.

Maple script #1 in Appendix A was used to calculate the free sulfuric acid molecules and the actual equilibrium partial pressure of water in this system. The equilibrium constants are from Chapter 4. It should be noted that the equilibrium constants above $n=7$ of $\text{H}_2\text{SO}_4 \bullet n\text{H}_2\text{O}$ were assumed to increase slightly (unlikely) from their $n=7$ value. This was accomplished by lowering ΔG negatively by 1 kcal/mol for hydrates above $n=7$ starting from the ΔG of hydration for $\text{H}_2\text{SO}_4 \bullet 7\text{H}_2\text{O}$. Substitution of the calculated free sulfuric acid molecules, the actual equilibrium partial pressure of water and the equilibrium constants into Equation 2-59 yields a C' of 1. A very different value obtained by Jaecker-Voirol et al.¹ which was on the order of 10^{-7} - 10^{-8} !

Let one consider the possibility of calculating a C' using values which have some random error. One can use Equation 2-60 on Equation 2-59 to determine the ability to calculate reliable values and to determine how sensitive Equation 2-59 is with respect to its variables. Maple script #2 in Appendix A calculates a propagation of error on the full formula of Equation 2-59 with respect to equilibrium constants, partial pressures of water and the number of free sulfuric acid molecules. Equation 2-59 is quite insensitive towards the error in the equilibrium constants. A change 10⁹ percent standard deviation error in the equilibrium constants results in about 0.01 % error in C' . It should be understood that such a vast change in the equilibrium constants will most definitely change the concentration of free sulfuric acid molecules and the actual equilibrium partial pressure of water. A similar finding for the standard deviation of free sulfuric acid molecule was also found. Very small standard deviations were assumed for the equilibrium partial pressure of water above a surface of water, P_w and P_1 . It should be noted that an order of magnitude change in the standard deviation of P_w or P_1 results in a slightly more than an order of magnitude change in C' . Now, even with these assumed very small standard deviations in P_1 and P_w , the propagated error for C' is orders of

magnitude larger than the value of 1. This shows that Equation 2-59 is practically useless unless P_w and P_1 are known down to near parts per billion accuracy. The new introduced coefficient C' which was meant to explain the failures of classical homogenous nucleation theory with respect to new particle formation, fails to do so in light of the new thermodynamic results in this thesis.

New Kinetic Models

This section will present the new kinetic ultrafine aerosol models derived from the *ab initio* and DFT results. A comparison to recent experimental observations of new atmospheric aerosols measurements will be presented.

Minor Kinetic Aerosol Model (KAM-)

The Minor Kinetic Aerosol Model (KAM-) is useful for the quantitative and qualitative description of new atmospheric aerosol formation. An OH profile is parameterized into the model. The OH profile is non-zero at 6:00, becomes zero at 18:00 and has a maximum of 10^7 cm^{-3} as shown in Figure 8-3. This range has been selected to correspond to the experimentally measured tropospheric OH profiles.^{11,12} All KAM-runs are at a temperature of 273 K and have initial concentrations of SO_2 at 30 ppt. Also, the initial concentration of O_2 in KAM- is $5 \times 10^{18} \text{ cm}^{-3}$ and H_2O at $5 \times 10^{16} \text{ cm}^{-3}$ (30% RH at 273 K). The formation of SO_3 involves the combination of SO_2 with OH:¹³



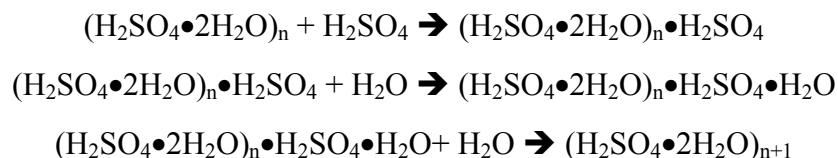
Whereby the HSO_3 is then oxidized into SO_3 :¹³



The SO_3 then combines with two H_2O 's to yield $\text{H}_2\text{SO}_4 \bullet \text{H}_2\text{O}$:¹⁴



For the hydrates of $\text{H}_2\text{SO}_4 \bullet n\text{H}_2\text{O}$, $n=0-7$, the forward hydration reactions and the reverse dehydration reactions are the same as those described in Chapter 5. To allow for the formation of $(\text{H}_2\text{SO}_4)_2 \bullet n\text{H}_2\text{O}$, it will be assumed that one of the conditions explained in Chapter 5 will be met in this system. The rest of the reactions involve the general scheme as mentioned in Chapter 5:



and all possible combinations between hydrated $(\text{H}_2\text{SO}_4 \bullet 2\text{H}_2\text{O})_n$ for n 0-200. Also, all species are slowly removed by sticking to background particles (dust, pollen, soot, etc.). The background particles are represented by a surface area usually expressed in $\mu\text{m}^2/\text{cm}^3$ and this sticking to the background particles can be represent by

$k_s = f(\text{oligimer})$, species + Pre-existing Surface Area \rightarrow Pre-existing Surface Area
where $f(\text{oligimer})$ is computed as:

$$f(\text{oligimer}) = \left(\frac{1}{4}\right) \cdot \delta \cdot A \cdot \left(\sqrt{\frac{8kT}{\pi m}}\right) \quad \text{Eqn. 8-1}$$

where T is temperature, m is mass of the oligimer, A is the surface area, δ is the sticking coefficient (which unity in KAM-), and k is Boltzmann's constant. All these reactions sum up to over 125,000 chemical reactions. Execution of BASIC program 1 in Appendix 2 will generate the entire described model. The models were then integrated with Kintecus V1.8.¹⁵

Model Runs

Seven models that had increasing background surface areas were generated. Each model was simulated over five days of model time. The results are shown in Figures 1-21. Each run has three plots associated with it. The first is a contour plot showing the concentration of all species as the simulation progresses through each day. The color legend and contours represent the order of magnitude of the concentration of a species in molecules/ cm^3 . The second shows multiple cut-away sections along the y-axis (diameters) of the contour plot. The legend shows the hour each color line represents on the second day. The top blue line (0th hour) is actually 24 hours into the run and the bottom yellow line (12th hour) is actually 36 hours into the run. The third associated plot shows the gas-phase precursor concentration plots, which is not shown in the contour or cut-away plot. It should be noted that these runs represent upper bounds for the concentrations of $(\text{H}_2\text{SO}_4 \bullet 2\text{H}_2\text{O})_n$, $n \geq 1$ since we are assuming irreversible steps that proceed at the full collision rate. Recently, Viggiano et al.¹⁶ found that most hydrated cluster ion-neutral reactions proceed at or near 0.7 times the collision rate, so the assumption that the forward reactions are near the collision rate should be good.

The first run starts with a background surface area of $0 \mu\text{m}^2/\text{cm}^3$ and its results are shown in Figures 8-1 to 8-3. Note the rapid explosion of particles as shown in Figure 8-1. Figure 8-1 shows a decrease in all concentrations and this is mainly due to the decrease in SO_2 concentration. Figure 8-2 clearly shows a constant almost linear background of aerosols from the 0th hour to the 6th hour. Particles under 1 nm diameter experience a rapid increase as the OH concentration increases after the 6th hour. Afterwards, within a few hours all particles show a markedly increase in concentration. The gas phase precursors (Figure 8-3) also show a very rapid increase as the OH level rises. Hydrates of $\text{H}_2\text{SO}_4 \bullet n\text{H}_2\text{O}$, $n \geq 5$ do not form. The complete absence of background particles allows most gas phase precursors to remain overnight.

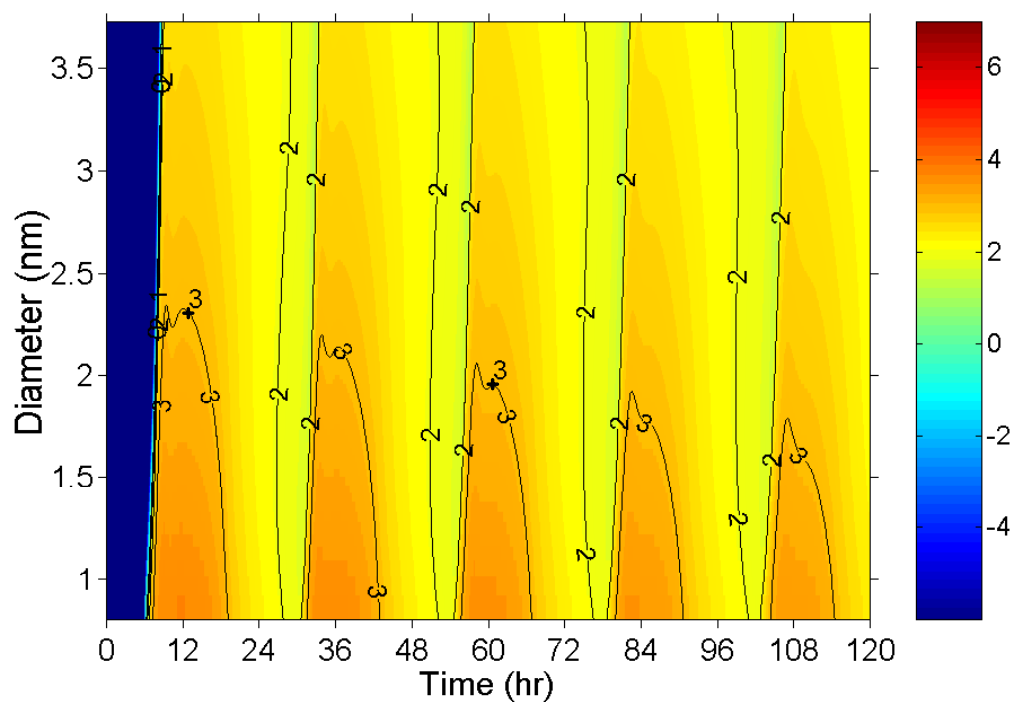


Figure 8-1. A KAM- model run with surface area at $0 \text{ um}^2/\text{cc}$.

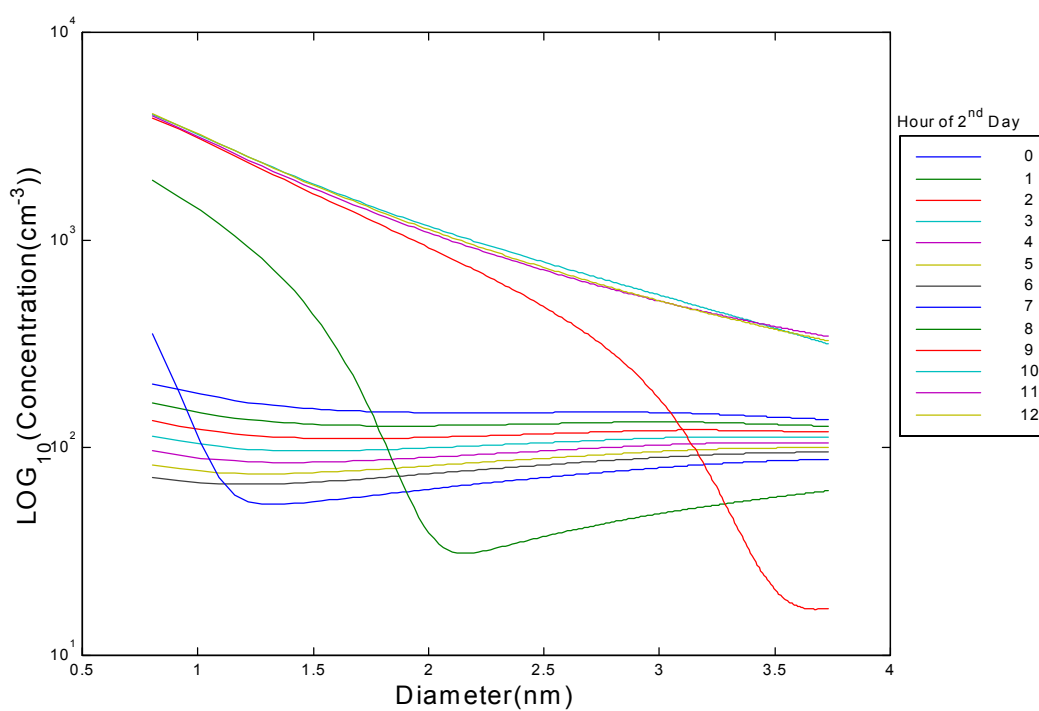


Figure 8-2. Cross sections of Figure 8-1 starting at 24:00 (0^{th} hour).

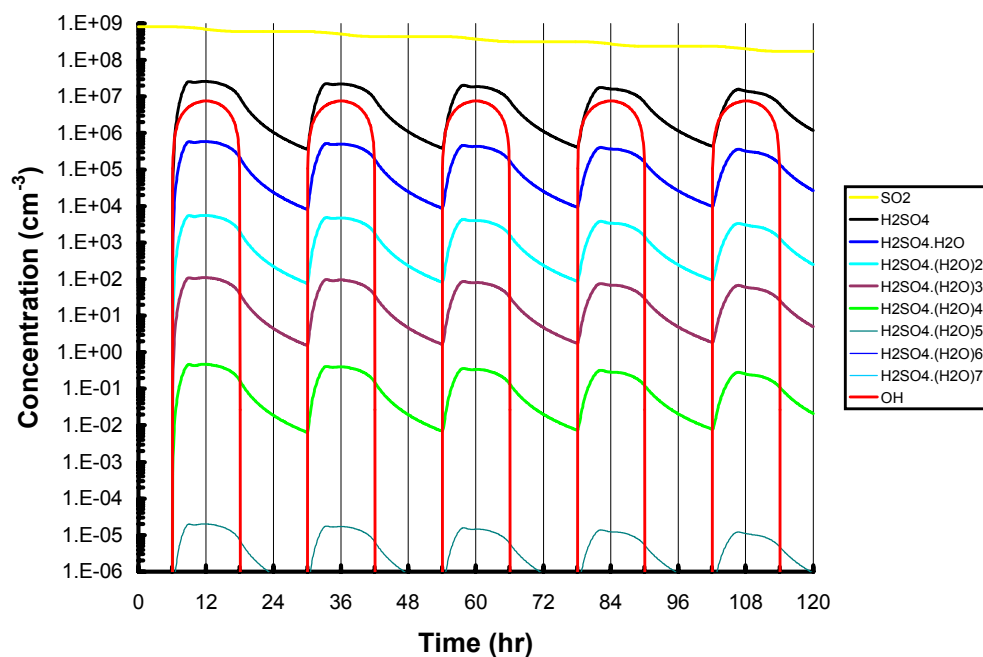


Figure 8-3. Gas phase precursor concentrations for Figure 8-1.

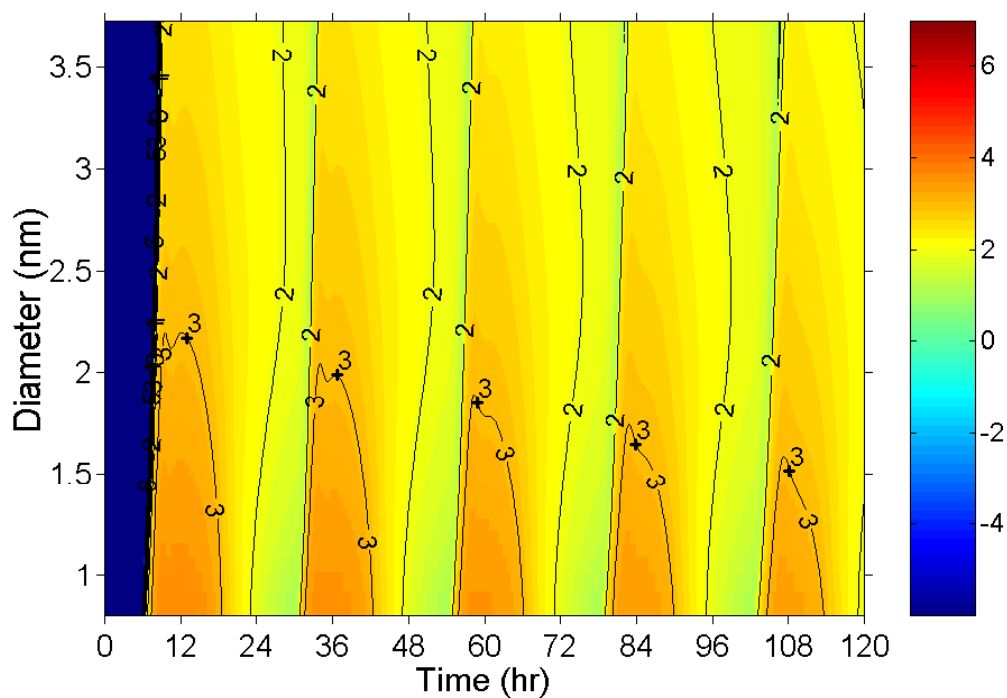


Figure 8-4 . A KAM- model run with surface area at $1 \mu\text{m}^2/\text{cc}$.

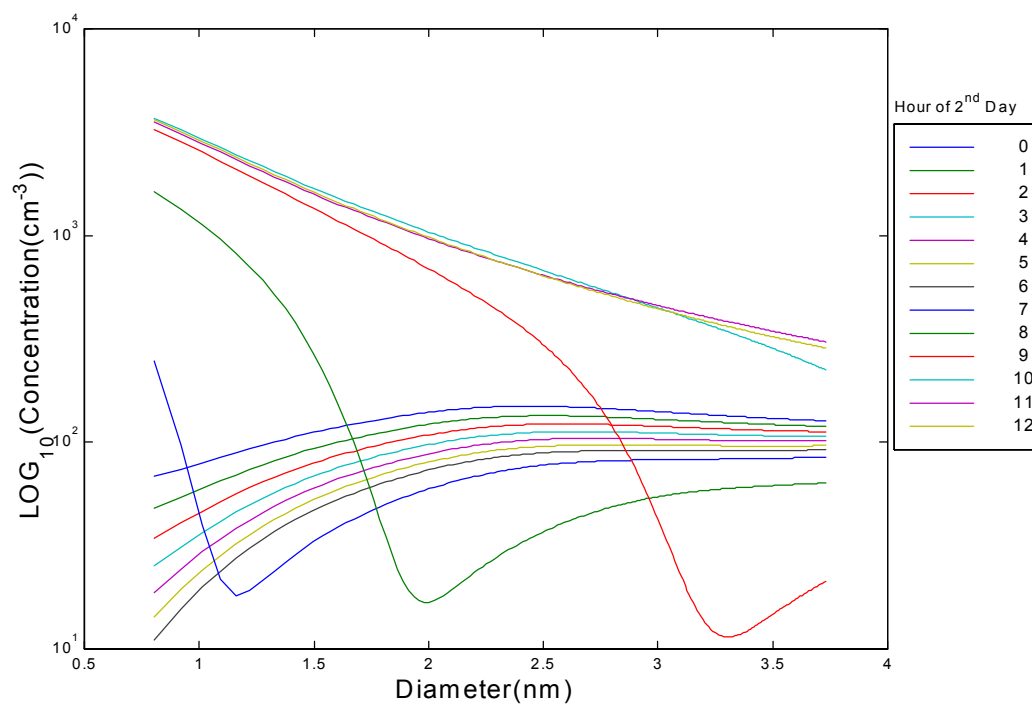


Figure 8-5. Cross sections of Figure 8-4 starting at 24:00 (0th hour).

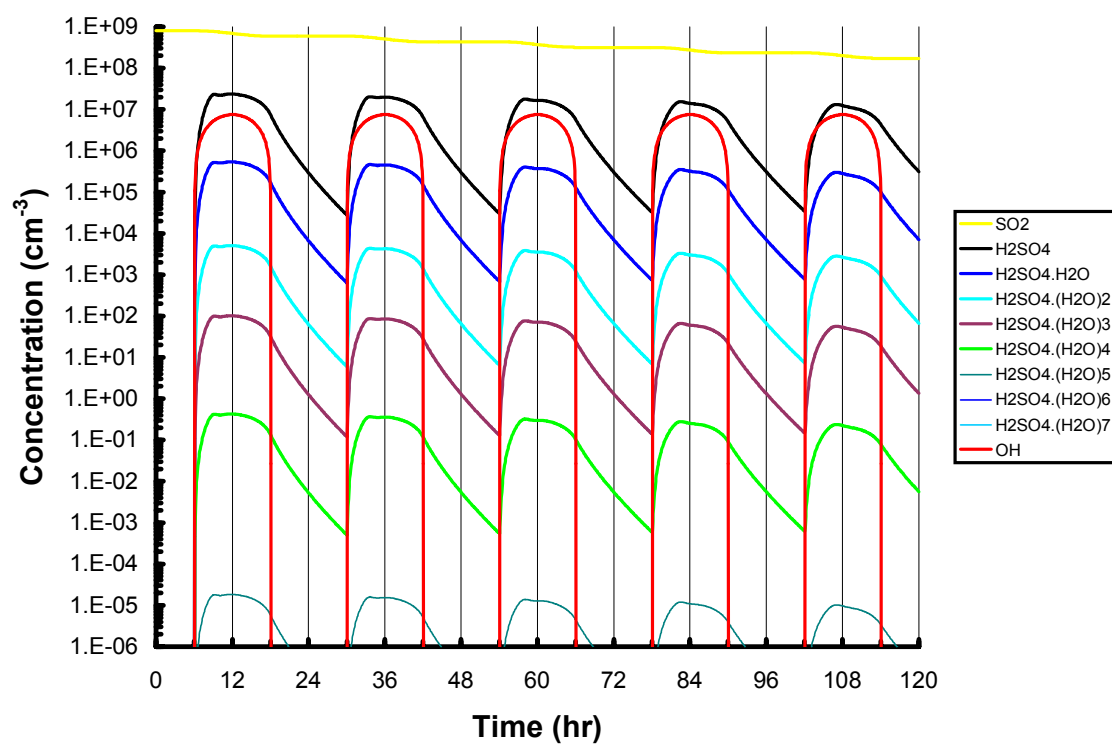


Figure 8-6. Gas phase precursor concentrations for Figure 8-4.

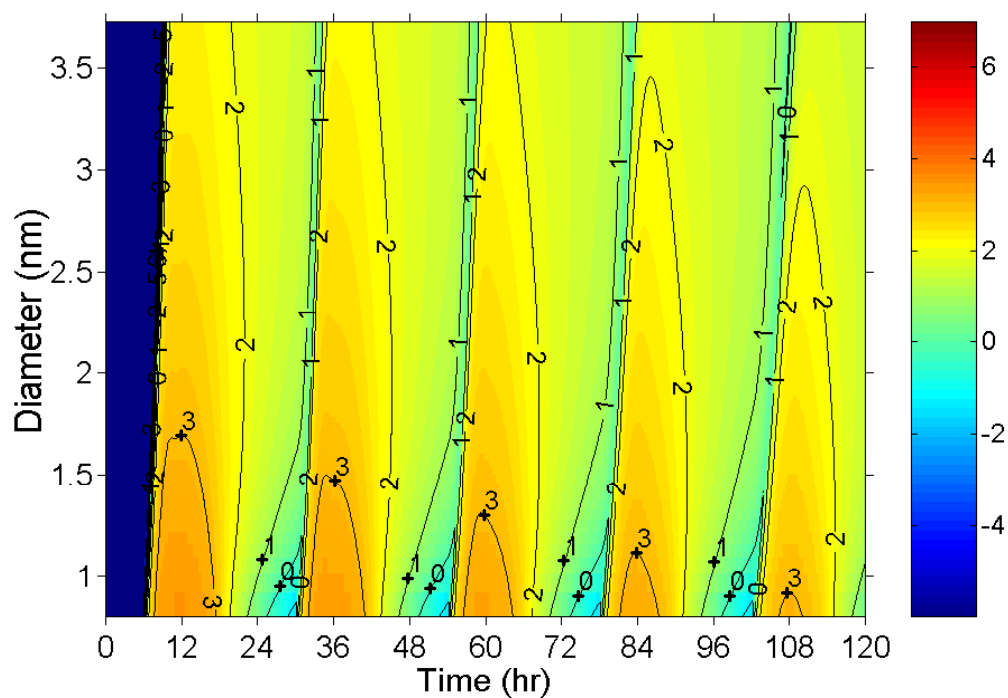


Figure 8-7. A KAM- model run with surface area at $5 \mu\text{m}^2/\text{cc}$.

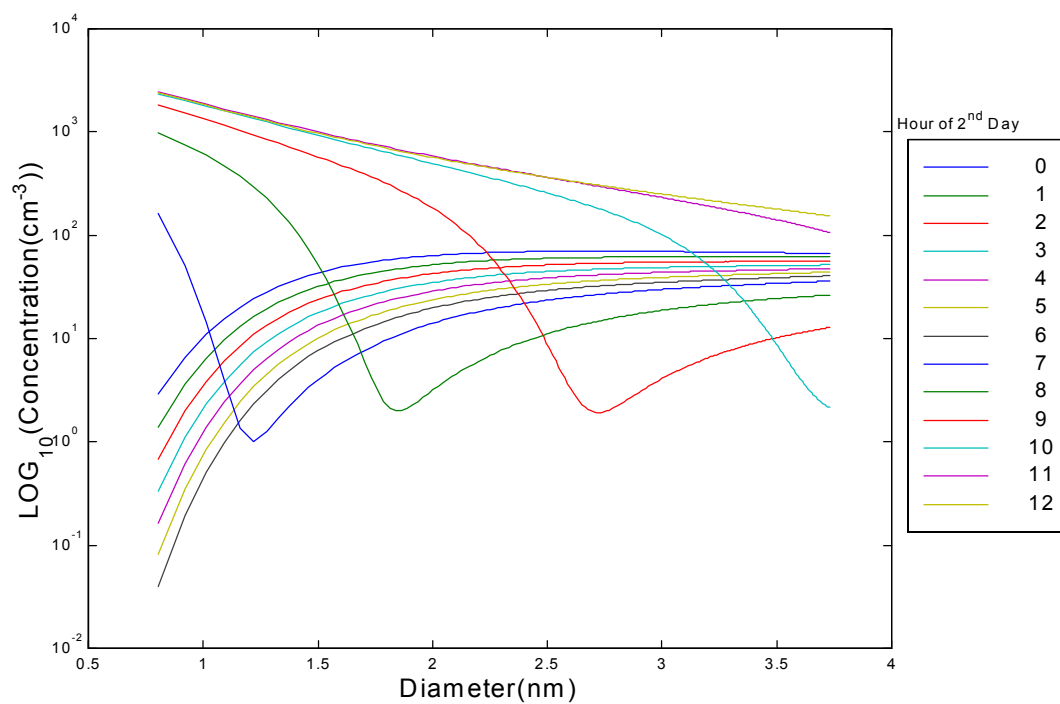


Figure 8-8. Cross sections of Figure 8-7 starting at 24:00 (0th hour).

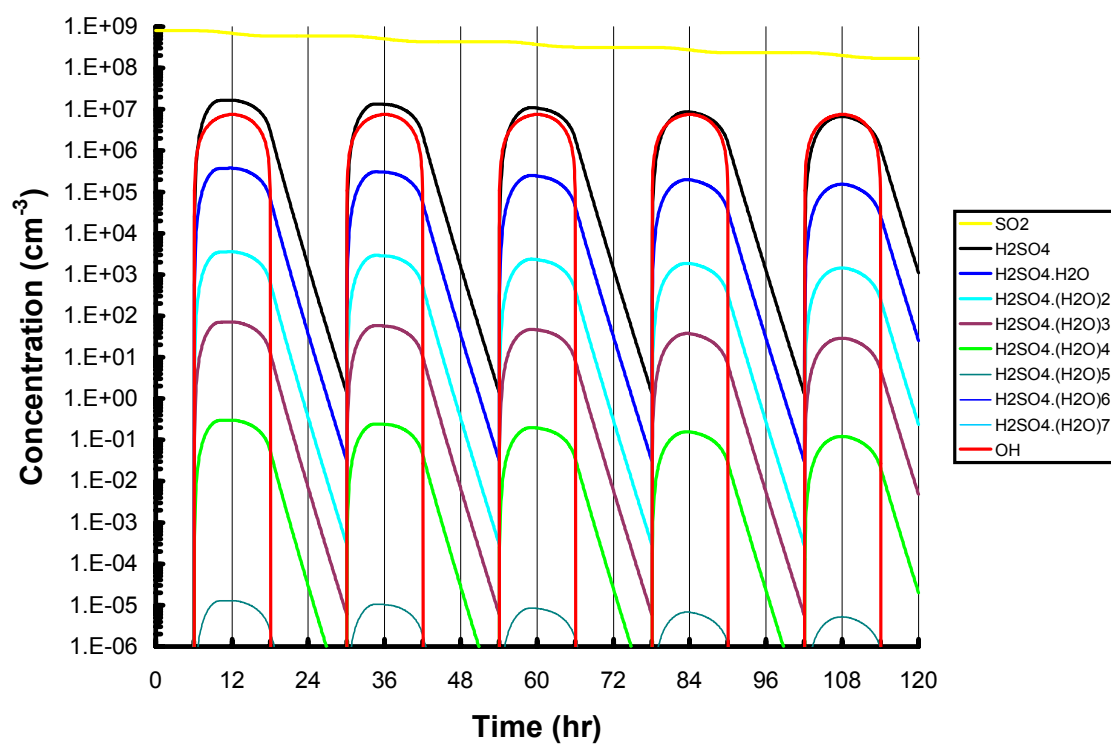


Figure 8-9. Gas phase precursor concentrations for Figure 8-7.

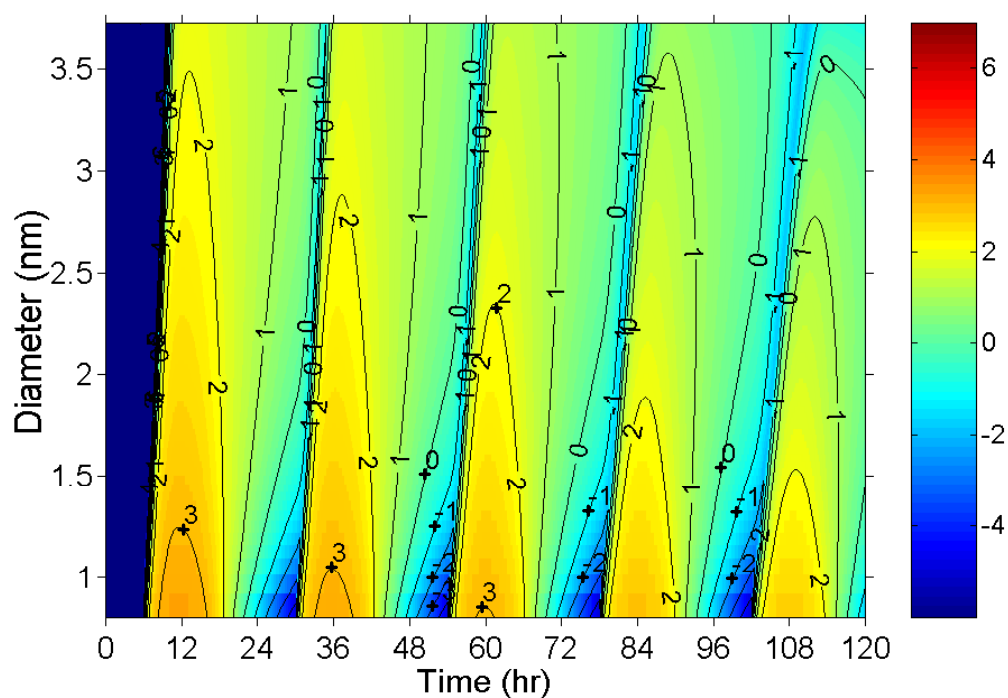


Figure 8-10. A KAM- model run with surface area at 10 $\mu\text{m}^2/\text{cc}$.

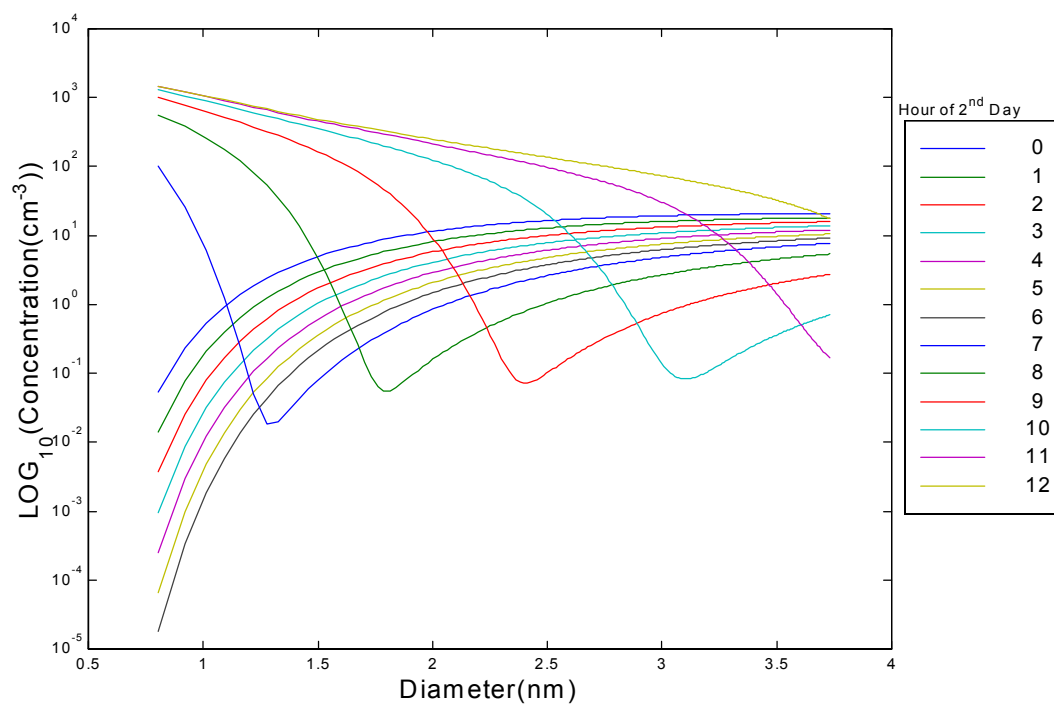


Figure 8-11. Cross sections of Figure 8-10 starting at 24:00 (0th hour).

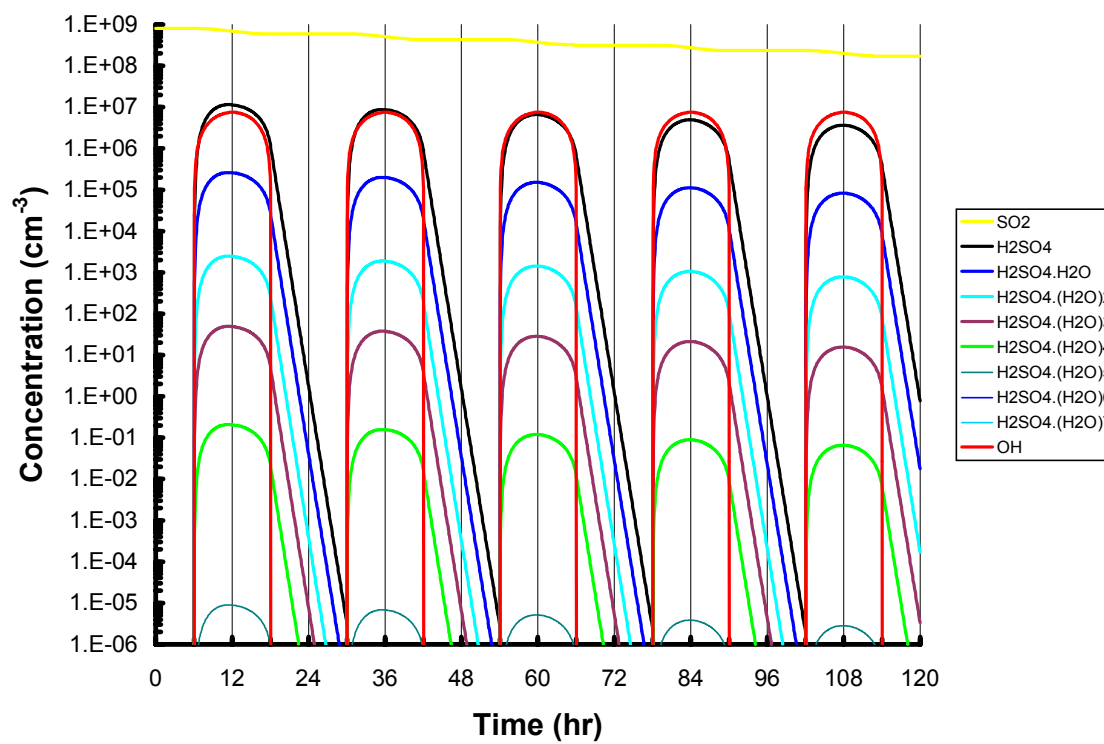


Figure 8-12. Gas phase precursor concentrations for Figure 8-10.

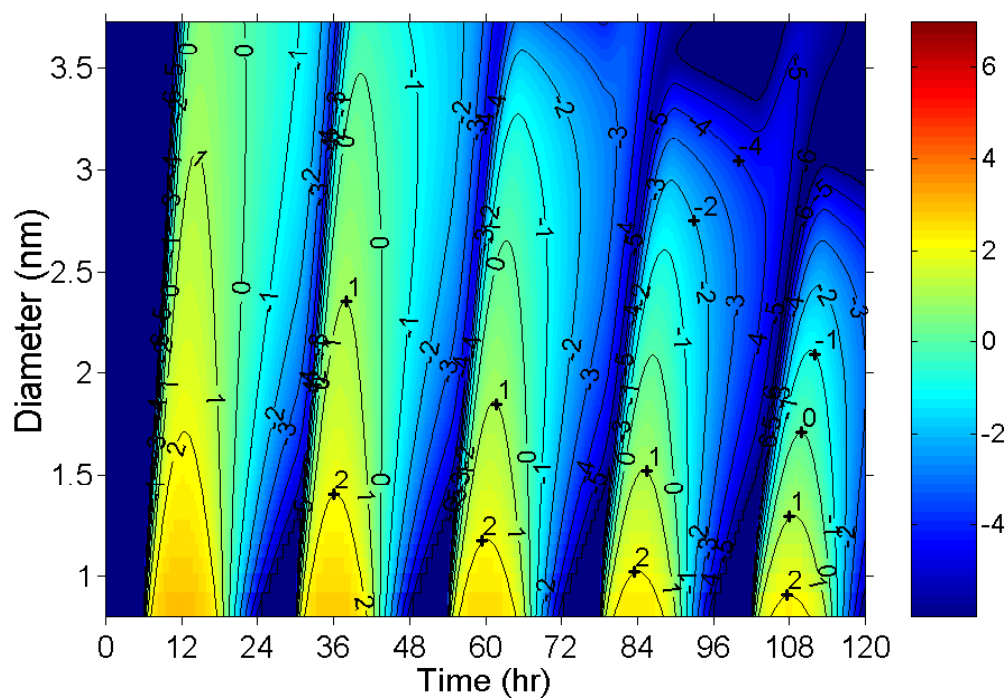


Figure 8-13. A KAM- model run with surface area at $20 \text{ } \mu\text{m}^2/\text{cc}$.

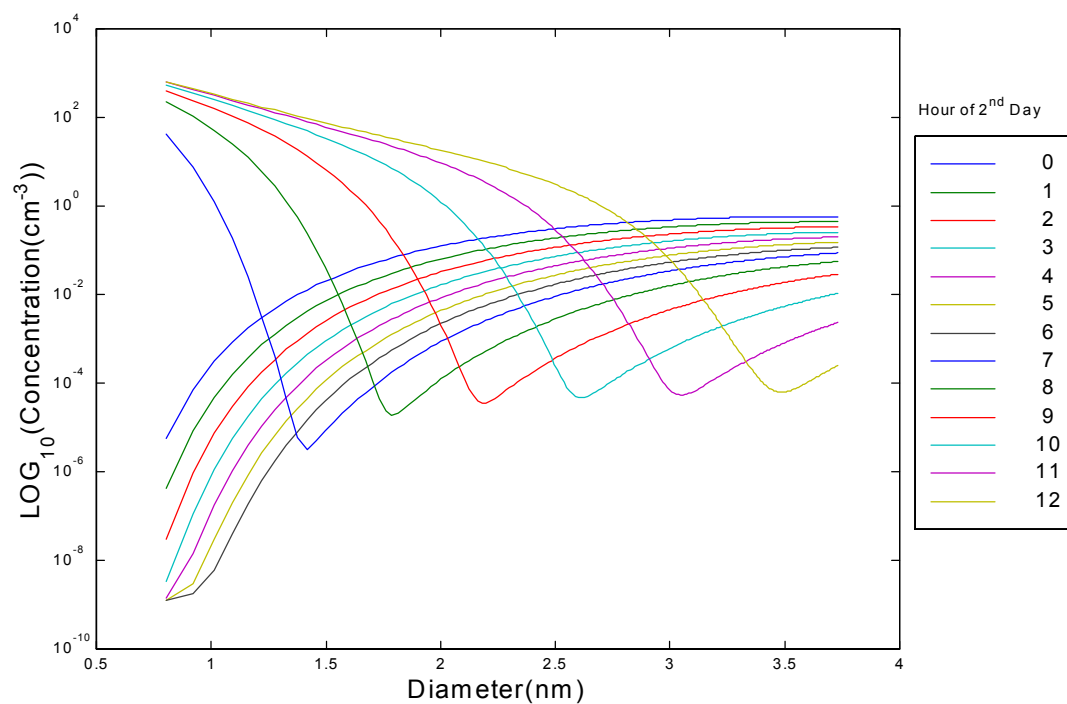


Figure 8-14. Cross sections of Figure 8-13 starting at 24:00 (0^{th} hour).

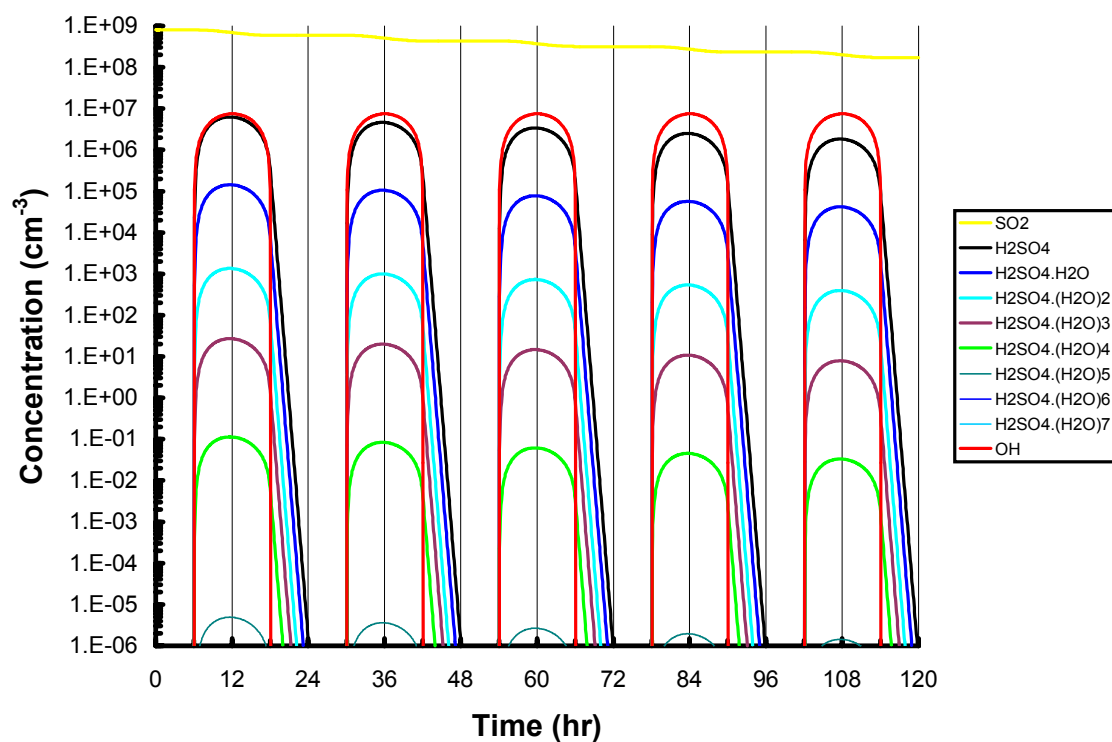


Figure 8-15. Gas phase precursor concentrations for Figure 8-13.

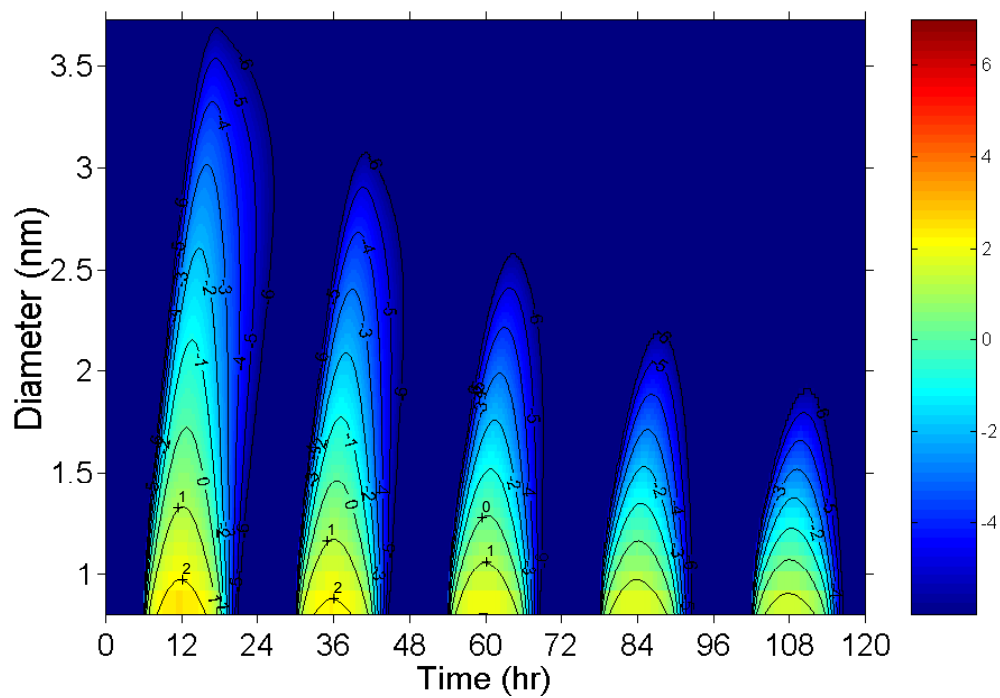


Figure 8-16. A KAM- model run with surface area at $40 \mu\text{m}^2/\text{cc}$.

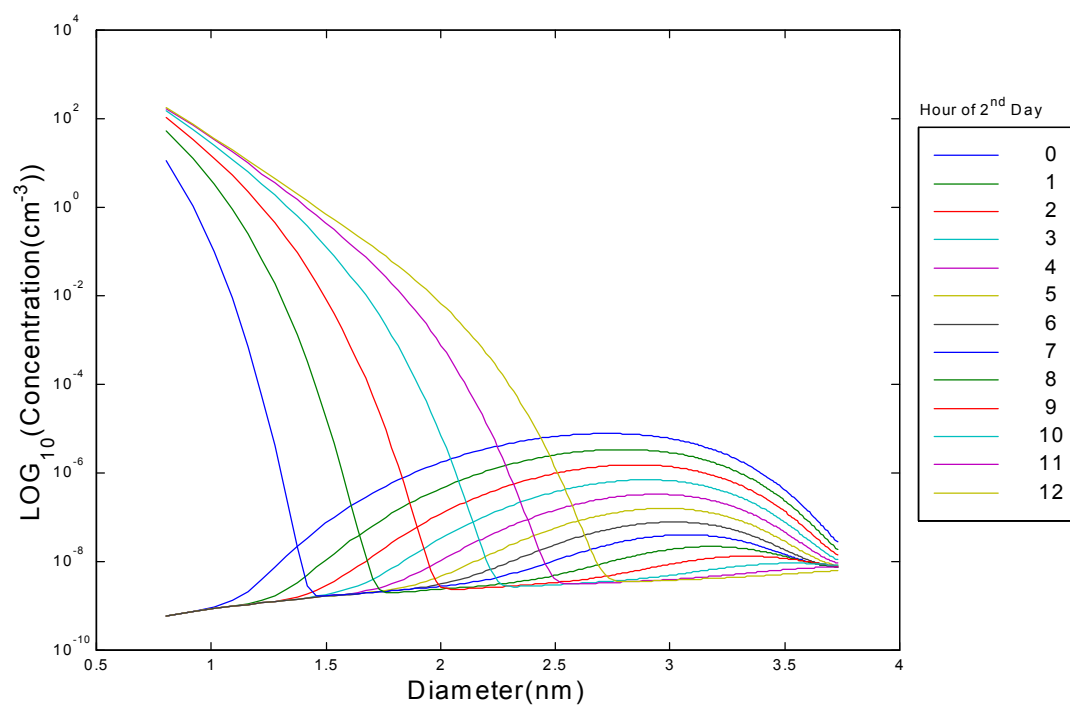


Figure 8-17. Cross sections of Figure 8-16 starting at 24:00 (0th hour).

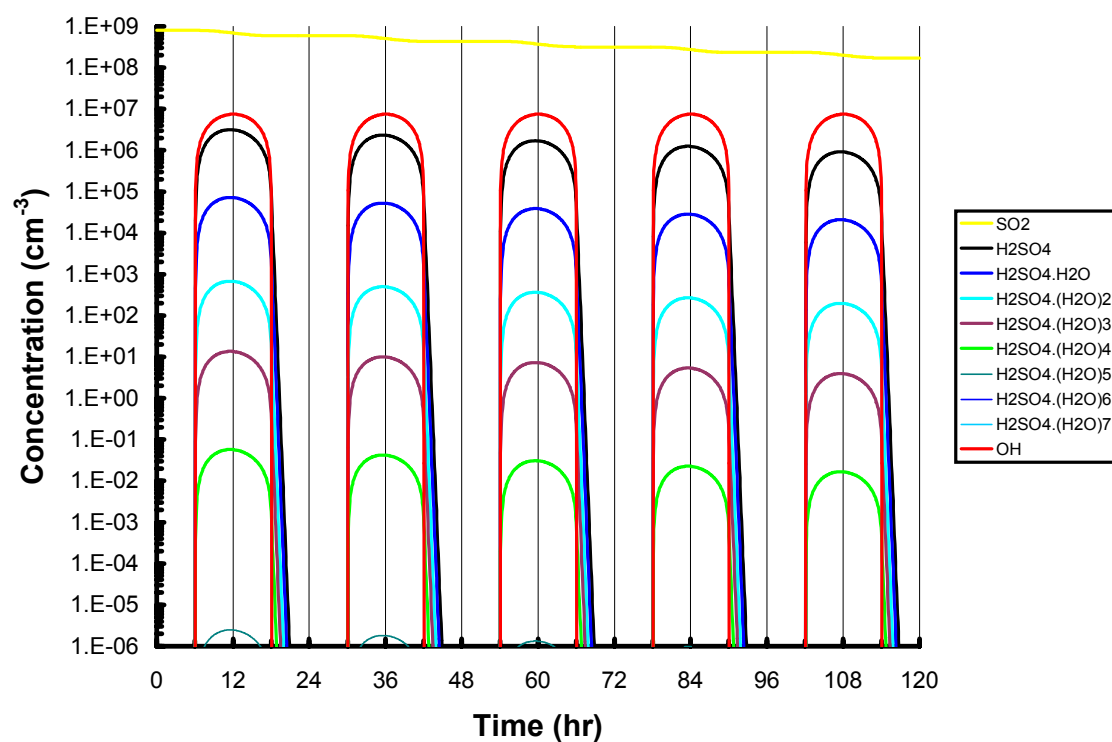


Figure 8-18. Gas phase precursor concentrations for Figure 8-16.

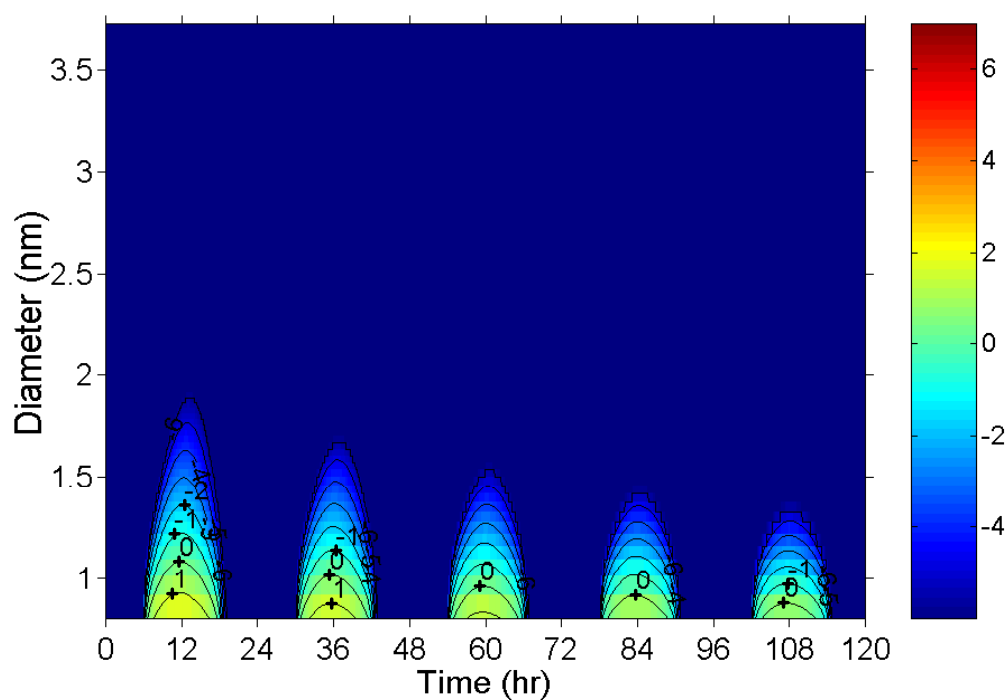


Figure 8-19. A KAM- model run with surface area at $80 \mu\text{m}^2/\text{cc}$.

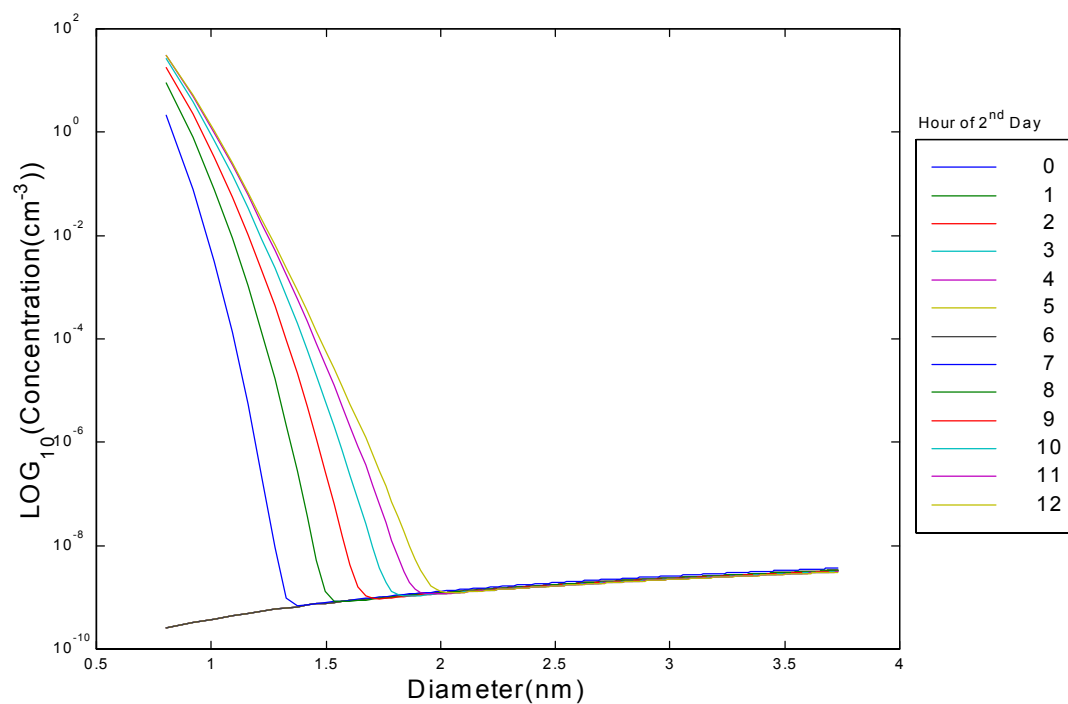


Figure 8-20. Cross sections of Figure 8-19 starting at 24:00 (0th hour).

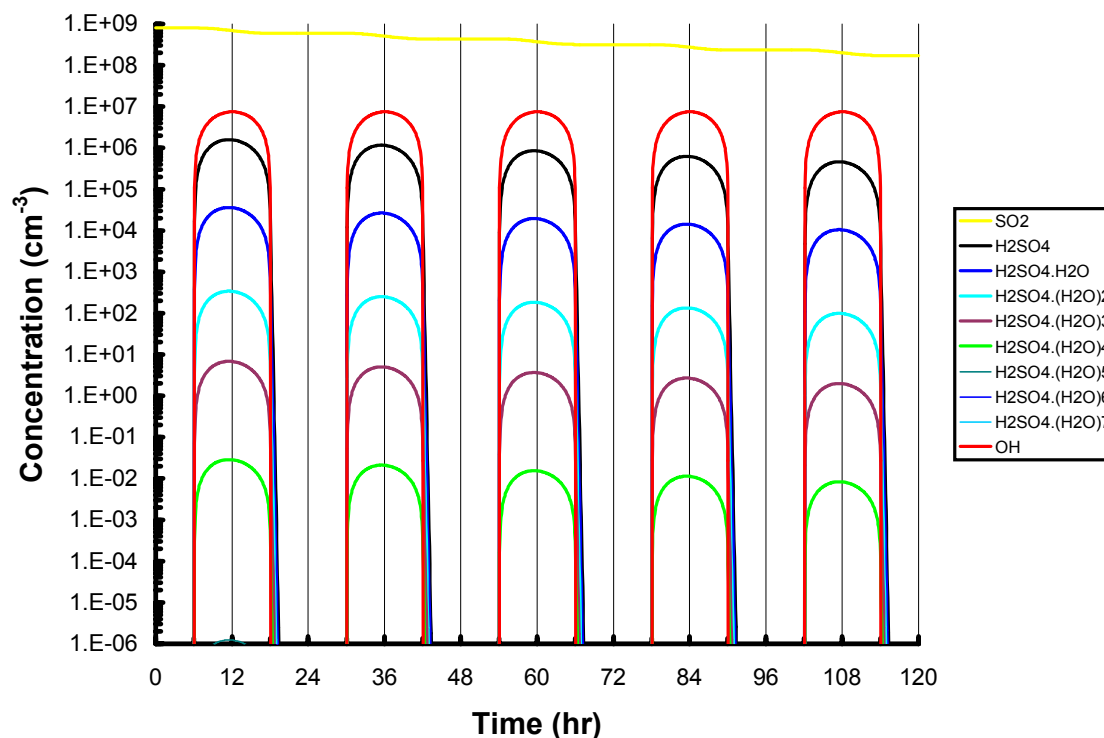


Figure 8-21. Gas phase precursor concentrations for Figure 8-19.

The second run has a background surface area of $1 \mu\text{m}^2/\text{cm}^3$ and its results are shown in Figures 8-4 to 8-6. Again, note the rapid explosion of particles as shown in Figure 8-4. In actually, there is little difference between the first run of $0 \mu\text{m}^2/\text{cm}^3$ background surface area and this run.

The third run has a background surface area of $5 \mu\text{m}^2/\text{cm}^3$ and its results are shown in Figures 8-7 to 8-9. Again, note the rapid explosion of particles as shown in Figure 8-7. Some blue appears at night in the smallest particles. It appears that there is enough background surface area to quickly reduce the concentration of the smallest particles. The large particles have a very slow speed and this prevents them from colliding with background surface area and so do not completely disappear. This is also very apparent in Figure 8-8, which shows the largest particles to have a constant linear distribution among them at around 60 cm^{-3} . Figure 8-9 shows that the gas-phase precursors also disappear at night, except for H_2SO_4 .

The fourth run has a background surface area of $10 \mu\text{m}^2/\text{cm}^3$ and its results are shown in Figures 8-10 to 8-12. Again, note the rapid explosion of particles as shown in

Figure 8-10. The blue that appears at night is now a deeper blue indicating a further decrease of the concentration of particles. This decrease in concentration is even more prevalent for the smallest particles. Again, it appears that there is enough background surface area to quickly reduce the concentration of the smallest particles. Figure 8-11 also shows this reduction of concentration. Moreover, Figure 8-11 shows that the largest particles continue to have a constant linear distribution among them at around 10 cm^{-3} . All the gas phase precursors reach a concentration of 0 cm^{-3} within a few hours as depicted in Figure 8-12.

The fifth run has a background surface area of $20 \mu\text{m}^2/\text{cm}^3$ and its results are shown in Figures 8-13 to 8-15. The formation of particles is only for particles that have a diameter under 3.5 nm as shown in Figure 8-13. When the SO_2 concentration is halfway depleted at 84 hours no particle formation happens above 2 nm. Interestingly, this is exactly what happens when background surface areas reach above $10 \mu\text{m}^2/\text{cm}^3$.^{12,17,18} Figure 8-14 shows that for a background surface area of $20 \mu\text{m}^2/\text{cm}^3$ none of the particles even reach 1 cm^{-3} at night. Figure 8-15 shows that all the gas phase precursors quickly reach a concentration of 0 cm^{-3} .

The sixth run has a background surface area of $40 \mu\text{m}^2/\text{cm}^3$ and its results are shown in Figures 8-16 to 8-18. The formation of particles is only for particles that have a diameter under 1.5 nm as shown in Figure 8-16. Figure 8-17 shows that there are no particles left at night. The gas phase precursors reach a concentration of zero at night very quickly. Hydrates of $\text{H}_2\text{SO}_4 \bullet n\text{H}_2\text{O}$, $n \leq 2$, still form during the day.

The final run has a background surface area of $80 \mu\text{m}^2/\text{cm}^3$ and its results are shown in Figures 8-19 to 8-21. Note that the only particle forming is $(\text{H}_2\text{SO}_4 \bullet 2\text{H}_2\text{O})_2$ and $(\text{H}_2\text{SO}_4 \bullet 2\text{H}_2\text{O})_3$ during the afternoon. When the concentration of SO_2 reaches about 1/5 its starting value at 108 hours there is practically no formation of any particles. Figure 8-20 shows no particle production for all diameters except in afternoon when the concentration of $(\text{H}_2\text{SO}_4 \bullet 2\text{H}_2\text{O})_2$ and $(\text{H}_2\text{SO}_4 \bullet 2\text{H}_2\text{O})_3$ is on the order of 10 cm^{-3} . Figure 8-21 shows that all the gas phase precursors very closely follow the OH curve and where hydrates of $\text{H}_2\text{SO}_4 \bullet n\text{H}_2\text{O}$, $n \leq 2$, still form during the day.

If we sum the concentration for all species between 3-4 nm diameters we can compare it to recent experimental observations of Weber et al.¹⁹ Figure 8-22 shows this summation for runs 2-5 over 24 to 48 hours. Weber et al. sampled sulfate aerosol particles in tropospheric air downwind from the Macquarie Island, Australia as part of ACE-1 (Aerosol Characterization Experiments 1). Their sample numbers 233, 239, 240 and 242 have concentrations of particles in the 3-4 nm range 300, 500, 2000 and 100 particles/cm³, respectively. Measurements were made at a temperature of 4.4° C, 59% RH and a local time of 11:52 to 14:44, which would correspond to 36 to 39 hours of simulation time in Figure 8-22. Weber et al. do not report surface areas, but it is commonly known that if sticky surface areas go above 10 μm²/cm³, particles do not form. An assumption is made that surface areas are under or near 10 μm²/cm³. The 10 μm²/cm³ plot on Figure 8-22 shows good agreement with the particle measurements of Weber et al., especially if one considers that the paper reports overall losses of 3 nm particles of 50%, which is not compensated in the results of the paper. In addition, their particle counter will give lower bounds towards the true concentration of particles in the 3-4 nm range. Moreover, the H₂SO₄ measurements are in the order of 1 x 10⁷ molecules/cm³, which are in excellent agreement with the H₂SO₄ calculated concentrations shown in Figure 8-22 for the 10 μm²/cm³ run.

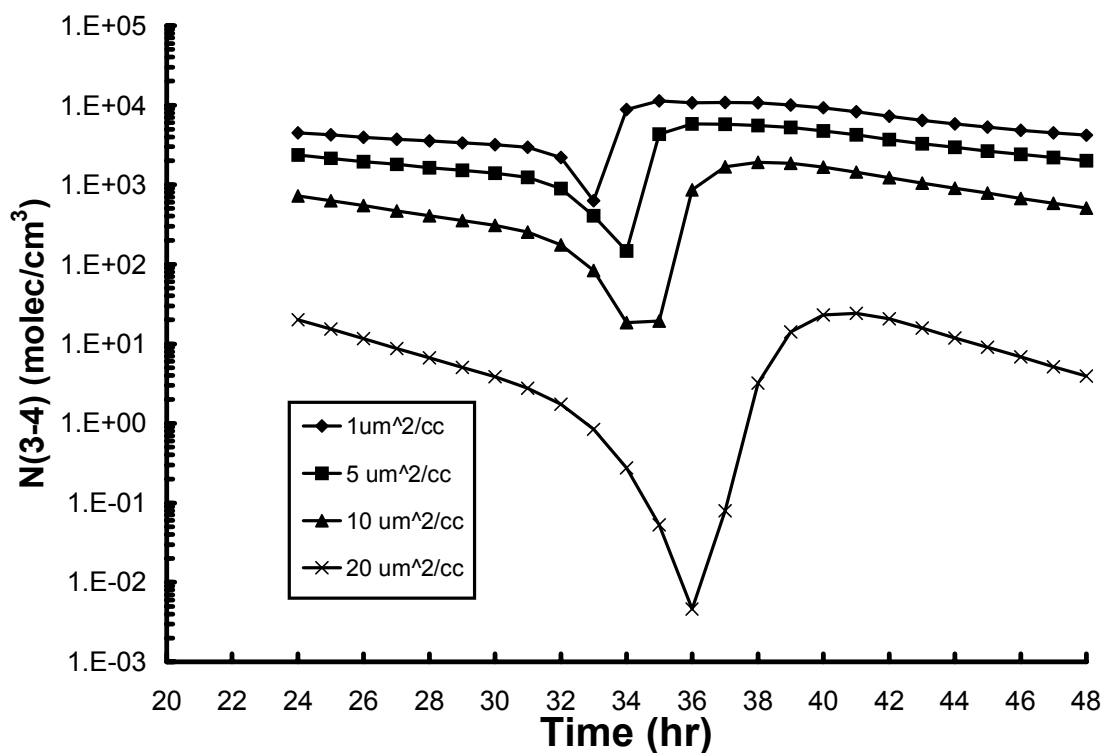


Figure 8-22. Summation of particles/molecules, for the hour shown, that have a diameter between 3 and 4 nm.

Model for New Particle Formation Next to Cumulus Clouds

One can now try to model the large particle production found next to cumulus clouds. New particle production can happen above cumulus/cumuliform clouds and in the detrainment of air from those clouds too.^{17,20} A model of an air parcel that is entrained from the boundary layer into a cumuliform cloud where it is later detrained from the “anvil” end is shown in Figure 8-23.

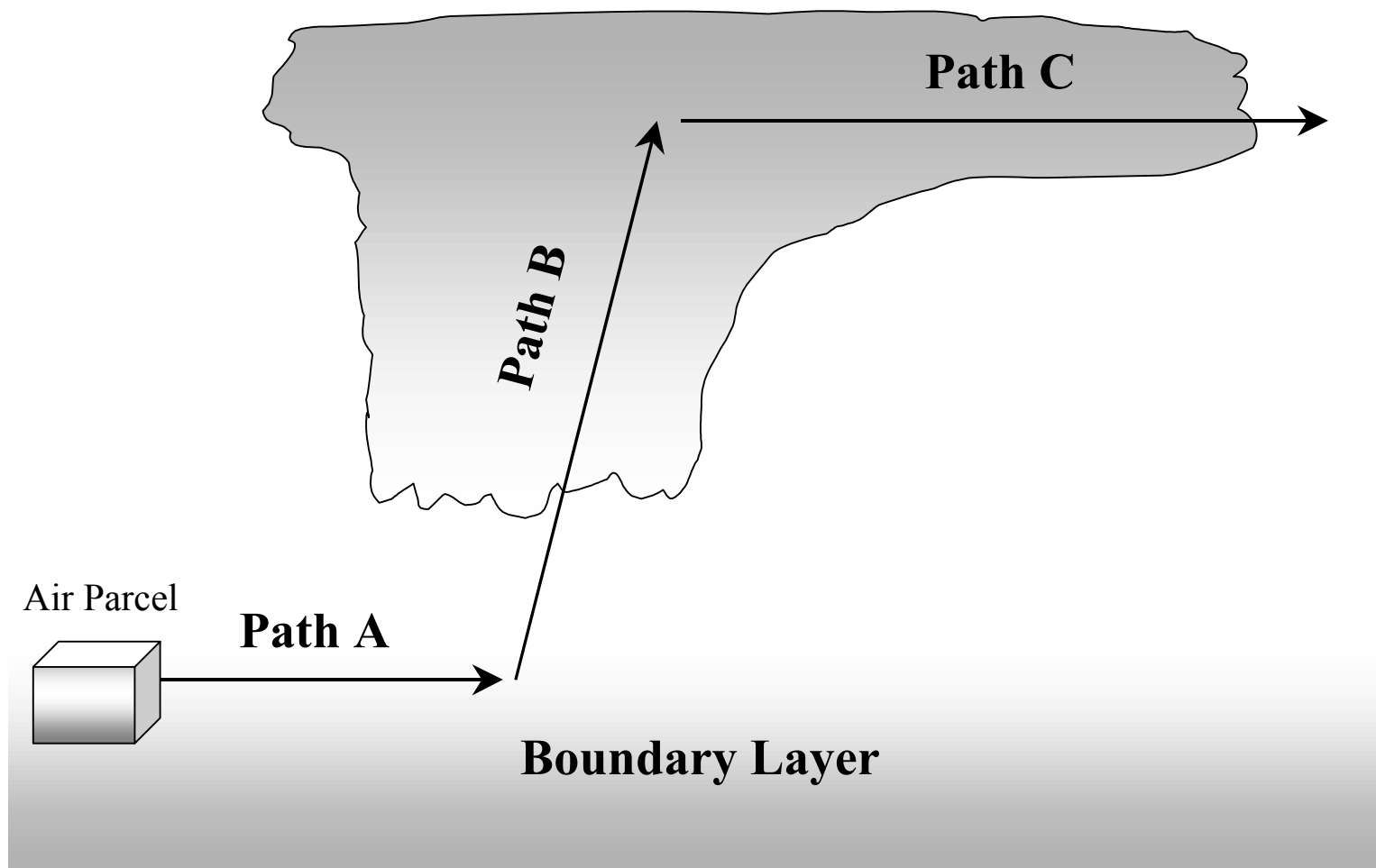


Figure 8-23. The path of an air parcel that is used in the model for new particle formation next to cumulus clouds.

Path A depicts the air parcel originating near the boundary layer at 9:00 AM local time (0:00 model time), where background surface area is relatively high to prevent new nucleation of particles even though there is enough SO_2 (30 ppt) to start nucleation. This air parcel becomes entrained into a nearby cumuliiform cloud (Path B) where the background surface area is absorbed onto the large ice crystals present inside the cloud. Most of the SO_2 is not absorbed onto the crystals and so, consequently, transverse through the cloud detrained at the “anvil” end of the cloud. Once the air parcel is detrained from the cloud (Path C), free from background surface area, rapid nucleation happens. The following model incorporates this entire process by taking into account:

- 1) The drop in temperature as the air parcel increases is altitude.
- 2) Decrease of relative humidity as the temperature drops.
- 3) The increase in the relative humidity as the air parcel enters the cloud.
- 4) The increase in surface area as the air parcel enters the cloud, followed by a large decrease in surface area as the air parcel is detrained from the cloud.
- 5) The varying OH concentration as the day progresses.

This is all parameterized as shown in Figures 24 to 27. In addition, the rate constants are now varying during the model since the temperature is no longer a constant. This can be included in the model by trivially casting Equation 2-54 into Equation 2-53, which is placed into Equation 2-56 and easily solved by Kintecus V1.78¹⁵. The entire model (125,000+ chemical reactions) is created by BASIC program #2 in Appendix B.

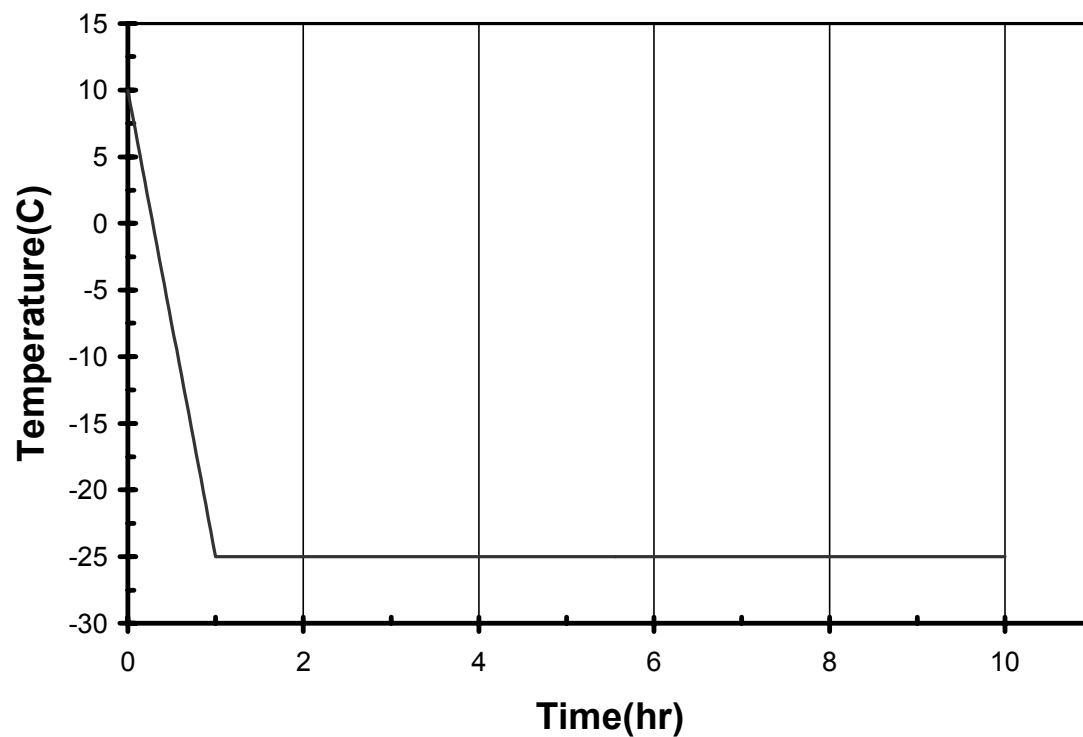


Figure 8-24. Temperature parameterization that is used in the model for new particle formation next to cumulus clouds.

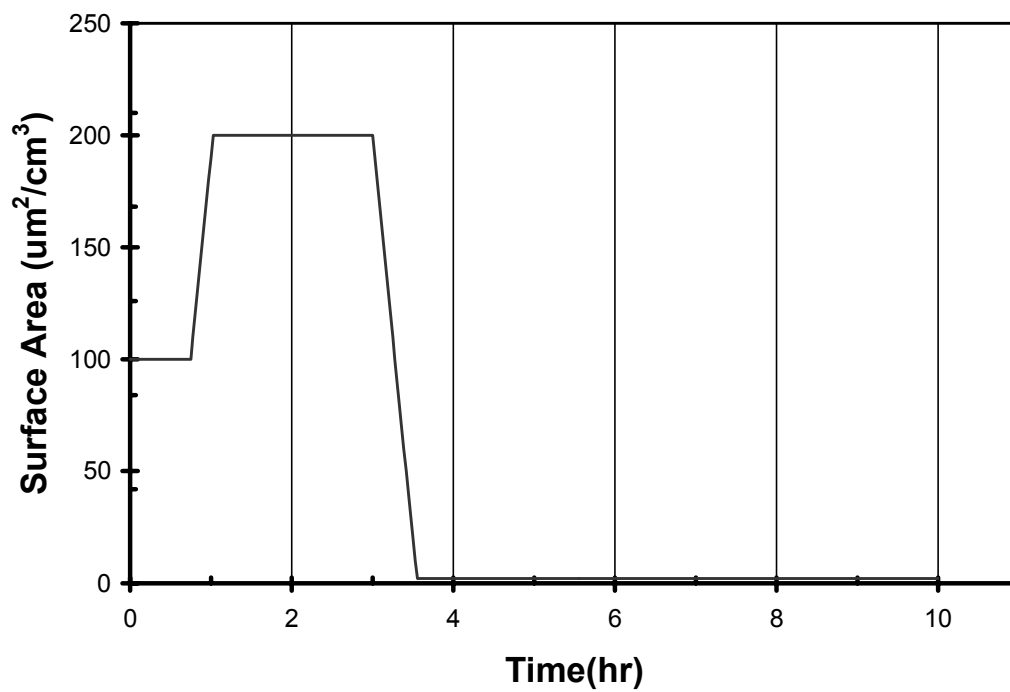


Figure 8-25. Surface area parameterization that is used in the model for new particle formation next to cumulus clouds.

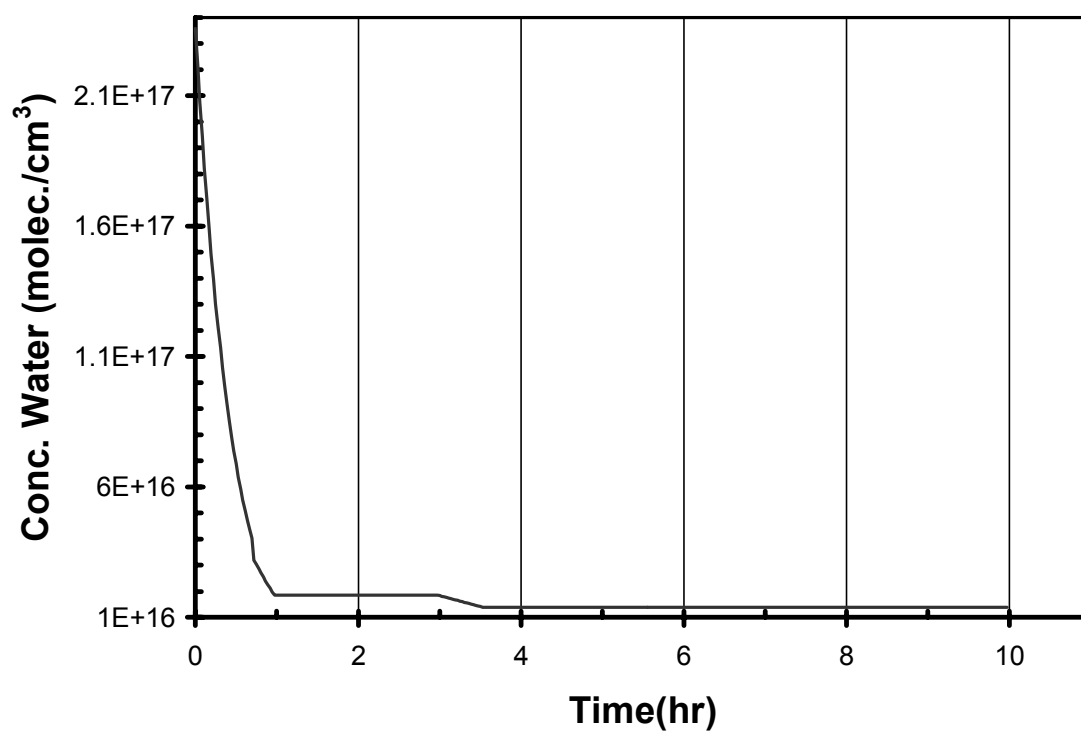


Figure 8-26. Water vapor concentration parameterization that is used in the model for new particle formation next to cumulus clouds.

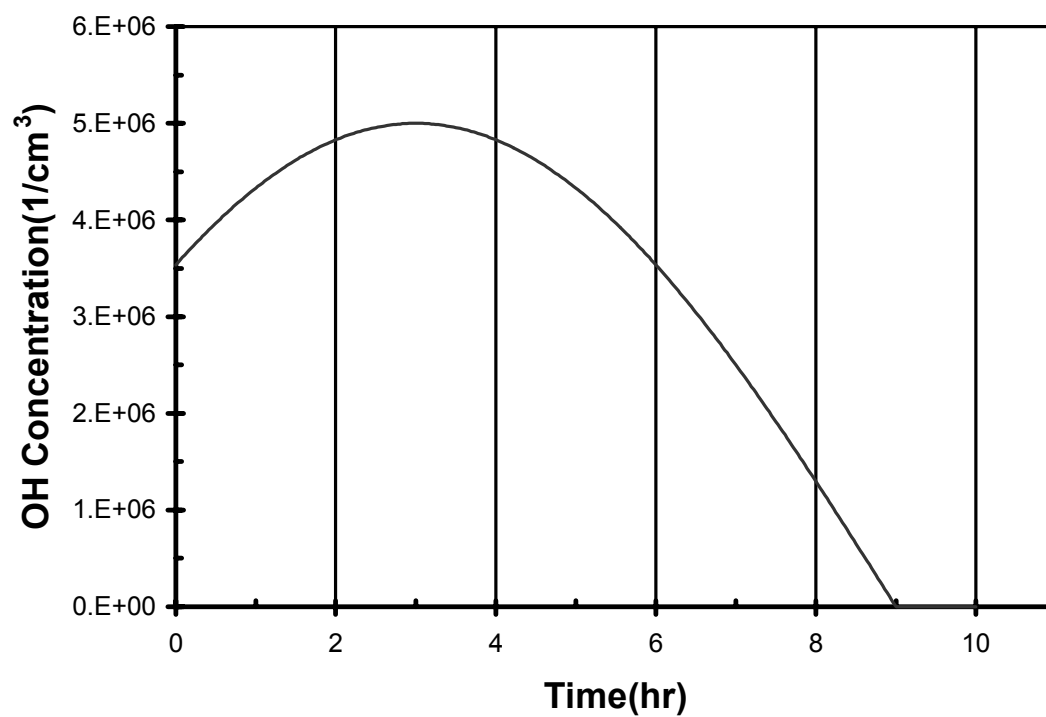


Figure 8-27. OH concentration parameterization that is used in the model for new particle formation next to cumulus clouds..

The results of the model are shown in Figure 8-26. Note the practically zero particle formation during the times 9:00 AM to 12:30 PM. Once the air parcel leaves the cloud, there is a very large increase in all the ultrafine aerosols as depicted by the yellow-orange throughout the plot.

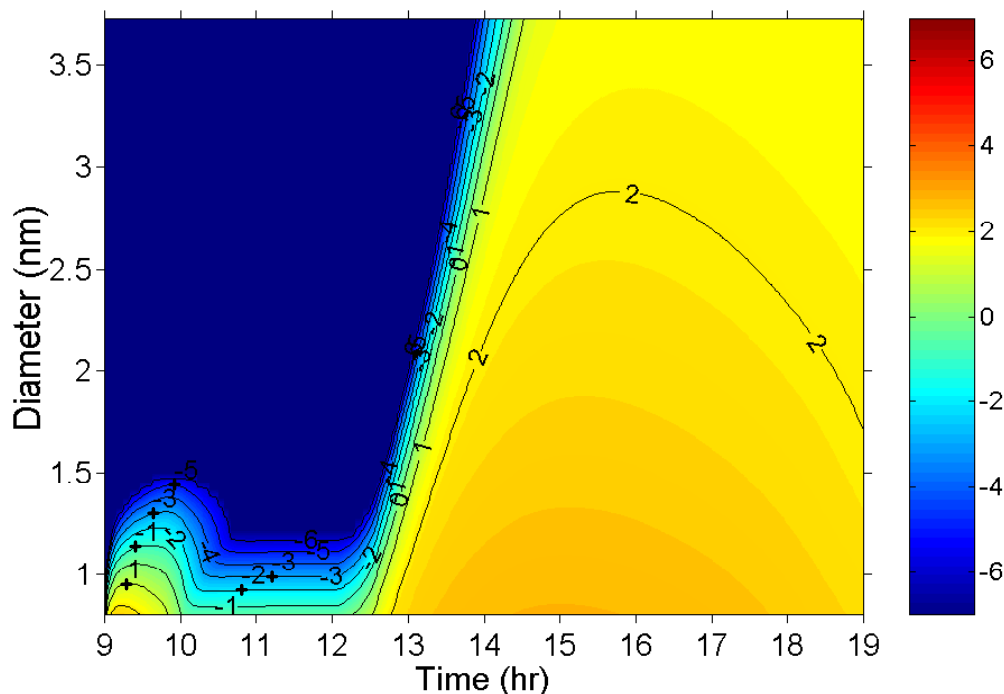


Figure 8-28. Resulting KAM- model output for new particle formation next to cumulus clouds.

Enhancing the Model (KAM+)

The minor Kinetic Aerosol Model (KAM-) described and used in various models above, calculates results for particles ≤ 3.80 nm diameter particle size. This diameter size refers to the molecular cluster $(\text{H}_2\text{SO}_4)_{200} \bullet (\text{H}_2\text{O})_{400}$. It is possible to simply extend BASIC program #1 in Appendix #2 to go beyond this, but the number of reactions grows about $O(N^2) = (3N)^2/2$, where N is the amount of H_2SO_4 's present in the cluster. To simply double the diameter from 3.8 nm to 7.6 nm, assuming the particles have a spherical shape with a density of 1.6 g/cc, would require over 12 million reactions! To calculate up to a size of 15.2 nm would require about 1×10^{19} reactions! Clearly, a better technique is required, and that is KAM+.

The enhanced model KAM+ is KAM- minus the surface area reactions and includes a binning scheme for reactions of oligimers which produce molecules larger than $(\text{H}_2\text{SO}_4 \bullet 2\text{H}_2\text{O})_{200}$. Each bin represents a range of oligimers that have a diameter that falls between the lower and upper limit of a particular bin size. Each bin has an average diameter size, $\langle d \rangle$, which can correspond to an average molecular weight, $\langle M_w \rangle$, by using the density of sulfuric acid solution and $V = (4/3)\pi r^3$. This leads to four different types of kinetic reactions:

- 1) oligimer + oligimer' \rightarrow C oligimer
- 2) oligimer + oligimer' \rightarrow C bin($\langle d \rangle$)
- 3) oligimer + bin($\langle d \rangle$)' \rightarrow C bin($\langle d \rangle$)''
- 4) bin($\langle d \rangle$) + bin($\langle d \rangle$)' \rightarrow C bin($\langle d \rangle$)''

Both KAM- and KAM+ incorporate reactions for case one which are reactions which produce oligimers that are as big as or smaller than $(\text{H}_2\text{SO}_4 \bullet 2\text{H}_2\text{O})_{200}$ (type 1 reactions). The reaction coefficient for the product, C, is always one in this case. For type 2 reactions which are reactions of oligimers which produce oligimers bigger than $(\text{H}_2\text{SO}_4 \bullet 2\text{H}_2\text{O})_{200}$, KAM+ determines what bin the product should fall into by summing the molecular weight of the reactant oligimers, determining a diameter for the molecular weight then finding out which bin has the range of diameters that can include the product's diameter. The product's coefficient is determined by the following formula:

$$C = \frac{\sum M_w(\text{reactants})}{\langle M_w(\text{product}) \rangle}$$

Now, for types 3 and 4 the calculation of C, the rate constants and the product bin is the same except $\langle M_w(\text{bin}) \rangle$ is used for the molecular weight. There are sinks for the oligimers and bins. In KIM- the oligimers are slowly depleted to a pre-existing surface area which would correspond to some distribution of much larger particles that are already present. In KIM+ the sinks are actually the much larger bins which react with the smaller bins and oligimers. There is no need to specify pre-existing particles to act as sinks in KIM+. KAM+ models can be created with Basic program #3 in Appendix B.

A sample run has been created with a bin size that goes to 30 nm diameter, and only has 80,000 reactions. It is shown in Figure 8-29. The KAM+ model run is for 15 days. One can see many new particles being form. If one looks closely, 2 1/3 modes are

“naturally” forming unlike past models which artificially induce modes by placing functions that mathematically produce modes that start, end and peak at certain values.^{21,22} The peak for one mode is around 2 nm, the other mode is around 9 nm, and a third of a mode starts at 15 nm and continues beyond 33 nm. KAM+ agrees at least qualitatively with the aerosols measurements of Weber et al^{12,23,24} who also measured a trimodal aerosol system with similar peaks.

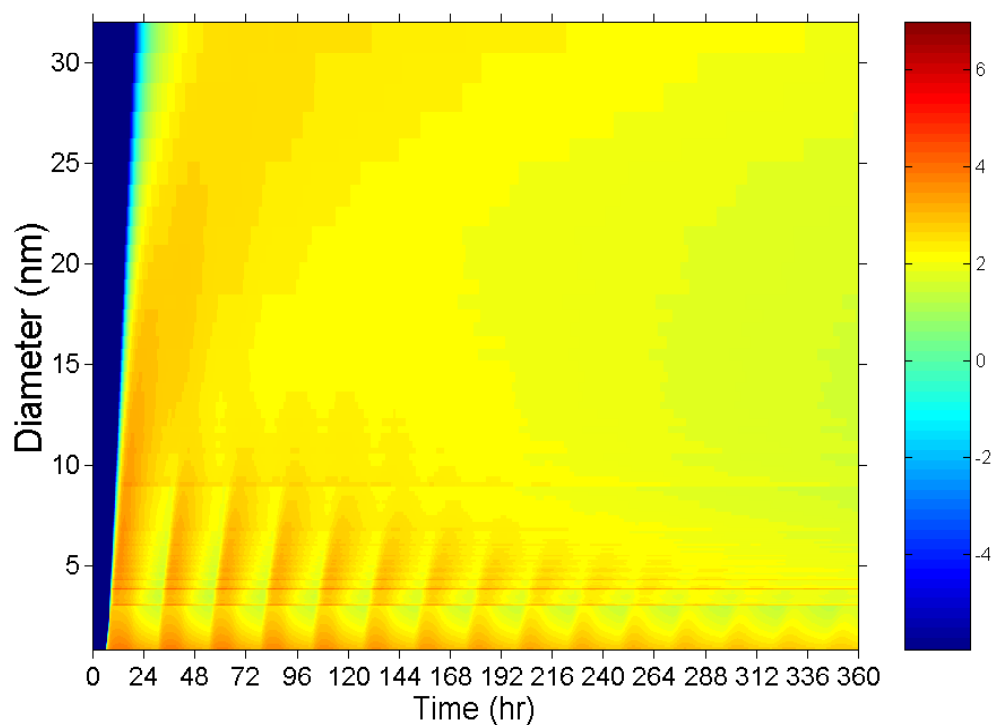


Figure 8-29. KAM+ model output. See text for full details.

Conclusion

It has been shown in this Chapter that previous published corrections applied to classical homogeneous nucleation theory are incorrect. In addition, new models that predict rapid aerosol formation have been shown. There are two models: a minor Kinetic Aerosol Model (KAM-) and a major Kinetic Aerosol Model (KAM+). KAM- is useful for accurate determination of sulfate aerosol formation up to 3.8 nm. While KAM+ can be used up to any size.

References

- (1) Jaecker-Voirol, A.; Mirabel, P.; Reiss, H. *J. Chem. Phys.* **1987**, *87*, 4849.
- (2) Jaecker-Voirol, A.; Mirabel, P. *J. Phys. Chem.* **1988**, *92*, 3518.
- (3) Jaecker-Voirol, A.; Mirabel, P. *Atm. Environ.* **1989**, *23*, 2053.
- (4) Taleb, D.-E.; McGraw, R.; Mirabel, P. *J. Geophys. Res.* **1997**, *102*, 12885.
- (5) McMurry, P. H.; Friedlander, S. K. *Atm. Environ.* **1979**, *13*, 1635.
- (6) McMurry, P. H. *Journal of Colloid and Interface Science* **1980**, *78*, 513-527.
- (7) Rao, N. P.; McMurry, P. H. *Aerosol Science and Technology* **1989**, *11*, 120-132.
- (8) McMurry, P. H. *Journal of Colloid and Interface Science* **1983**, *95*, 73-80.
- (9) Russell, L. M.; Pandis, S. N.; Seinfeld, J. H. *Journal of Geophysical Research-Atmospheres* **1994**, *99*, 20989-21003.
- (10) Alam, M. K.; Flagan, R. C. *J. Coll. Interf. Sci.* **1984**, *97*, 232-246.
- (11) Hard, T. M.; Chan, C. Y.; Mehrabzadeh, A. A.; Pan, W. H.; O'Brien, R. J. *Nature* **1986**, *322*, 617.
- (12) Weber, R. J.; Marti, J. J.; McMurry, P. H.; Eisele, F. L.; Tanner, D. J.; Jefferson, A. *J Geophys Res Atmos* **1997**, *102*, 4375-4385.
- (13) DeMore, W. B.; Sander, S. P.; Golden, D. M.; Hampson, R. F.; Kurylow, M. J.; Howard, C. J.; Ravishankara, A. R.; Kolb, C. E.; Molina, M. J. *Chemical Kinetics and Photochemical Data for Use in Stratospheric Modeling*; NASA: Jet Propulsion Laboratory, California Institute of Technology, 1992.
- (14) Jayne, J. T.; Poschl, U.; Chen, Y.-m.; David, D.; Molina, L. T.; Worsnop, D. R.; Kolb, C. E.; Molina, M. J. *J. Phys. Chem. A.* **1997**, *101*, 10000-10011.
- (15) Ianni, J. C. Kintecus; V1.78 ed.; <ftp://ccl.osc.edu/pub/chemistry/software/MS-DOS/kintecus/>; 1996.
- (16) Viggiano, A. A.; Seeley, J. V.; Mundis, P. L.; Williamson, J. S.; Morris, R. A. *J. Phys. Chem. A.* **1997**, *101*, 8275-8278.
- (17) Perry, K. D.; Hobbs, P. V. *Journal of Geophysical Research-Atmospheres* **1994**, *99*, 22803-22818.
- (18) Clarke, A. D.; Varner, J. L.; Eisele, F.; Mauldin, R. L.; Tanner, D.; Litchy, M. *J. Geoph. Res.* **1998**, *103*, 16397.
- (19) Weber, R. J.; McMurry, P. H.; Mauldin, L.; Tanner, D. J.; Eisele, F. L.; Brechtel, F. J.; Kreidenweis, S. M.; Kok, G. L.; Schillawski, R. D.; Baumgardner, D. *J. Geo. Res.* **1998**, *103*, 16385.
- (20) Hegg, D. A. *Geophys. Res. Lett.* **1991**, *18*, 995-998.
- (21) Pandis, S. N.; Russell, L. M.; Seinfeld, J. H. *Journal of Geophysical Research-Atmospheres* **1994**, *99*, 16945-16957.
- (22) Kreidenweiss, S. M.; Seinfeld, J. H. *Atmospheric Environment* **1988**, *22*, 283-296.
- (23) Weber, R. J.; McMurry, P. H. *Journal of Geophysical Research-Atmospheres* **1996**, *101*, 14767-14775.
- (24) Weber, R. J.; McMurry, P. H.; Eisele, F. L.; Tanner, D. J. *Journal of the Atmospheric Sciences* **1995**, *52*, 2242-2257.